Solar Energy 220 (2021) 258–268

Contents lists available at ScienceDirect

Solar Energy

journal homepage: www.elsevier.com/locate/solener

Formamidinium containing tetra cation organic–inorganic hybrid perovskite solar cell

Harish Singh [a,1], Pritam Dey [a,1], Shovon Chatterjee [b], Pratik Sen [b], Tanmoy Maiti [a,*]

[a] Plasmonics and Perovskites Laboratory, Department of Materials Science and Engineering, Indian Institute of Technology Kanpur, UP 208016, India
[b] Department of Chemistry, Indian Institute of Technology Kanpur, Kanpur – 208 016, UP, India

ARTICLE INFO

Keywords:
Organic-inorganic halide perovskites
Formamidinium
Transient absorption
Solar cell

ABSTRACT

ABX_3 perovskites offer the advantage of manipulating its properties by introducing multiple cations in B-site. Over the years, researchers used mixed B-site perovskites in oxide electronics to tune their electrical, magnetic properties. Here we used the triple cations at B-site in formamidinium based organometallic halide perovskite solar cell (PSC) in order to improve its degradation behavior with respect to heat and moisture. We synthesized halide based two hybrid perovskites viz., formamidinium sodium bismuth lead iodide [$NH_2CHNH_2(Na_{0.25}Bi_{0.25})Pb_{0.5}I_3$] and formamidinium potassium bismuth lead iodide [$NH_2CHNH_2(K_{0.25}Bi_{0.25})Pb_{0.5}I_3$] using solution chemistry. In order to decrease the content of toxic lead in these perovskites, trivalent bismuth was incorporated in the Pb-site. Monovalent sodium and potassium were used to maintain the charge neutrality of B-site, which has the formal valence of + 2 in these ABI_3 type perovskites. Both of these perovskites showed reasonable optical band gaps with good charge carrier lifetime suggesting it as potential candidates for solar energy conversion and provisionally we achieved power conversion efficiency $\eta = 0.52\%$. Moreover, superior thermal and moisture stability in these perovskites were observed in periodical structural and spectral analysis carried out by XRD, UV–Vis spectroscopy, time-correlated single photon counting (TCSPC) over the period of one month. Furthermore, ultrafast carrier dynamics in these perovskites were unraveled using femtosecond transient absorption studies. Our transient absorption kinetics data suggested more auger recombination and faster free electron-hole recombination process in FKBPI compared to FNBPI, which corroborates well with better energy conversion efficiency obtained in FNBPI based solar cell.

1. Introduction

Organic inorganic hybrid perovskite (OIHP) solar cells showed such a steep improvement (Grätzel, 2014; McGehee, 2014) in the power conversion efficiency over the last five years, that it is termed as the miracle photovoltaic material. Methylammonium lead halides (Green et al., 2014; Kojima et al., 2009; Lee et al., 2012; Burschka et al., 2013; Liu et al., 2013; Noh et al., 2013; Ball et al., 2013; Malinkiewicz et al., 2014) ($MAPbX_3$ where X = I, Cl, Br) are the most extensively studied perovskite materials owing to their high efficiency in energy conversion (Stranks and Snaith, 2015), and low fabrication cost. $MAPbI_3$ exhibits optical direct band gap of 1.55 eV (absorption edge at 800 nm) with the light absorbance in the entire visible spectrum (Jiang et al., 2016). However, considering the toxic and environmentally hazardous nature of lead, it is of prime concern to develop a lead-free perovskite solar cell material. Moreover, these materials suffer from poor moisture as well as thermal stability (Habisreutinger et al., 2014). In the presence of moisture, these materials degrade in the form of yellow PbI_2, which is a carcinogen. Hence the development of novel organometallic halide-based perovskite material is necessary to counter the degradation behavior of perovskite photo absorbers without compromising its high absorption coefficient. It was already reported that the compositional engineering (Comin et al., 2015) at halide site in $MAPbX_3$ helped in tuning its band gap. Similarly, the replacement at the A site by formamidinium (FA^+) cation remained one of the most popular choices (Fang et al., 2016; Han et al., 2016; Ma et al., 2017; Weller et al., 2015). The use of FA^+ results closed pack structure and exhibits lower band gap (Jeon et al., 2015) (1.48 eV, absorption edge at 840 nm) compared to that of $MAPbI_3$. $FAPbI_3$ exhibits two different phases, α-$FAPbI_3$ (black) and δ-$FAPbI_3$ (yellow) (Zhou et al., 2016). α-phase exhibits perovskite

* Corresponding author.
E-mail address: tmaiti@iitk.ac.in (T. Maiti).
[1] Equal contribution.

https://doi.org/10.1016/j.solener.2021.03.031
Received 24 December 2020; Received in revised form 24 February 2021; Accepted 13 March 2021
Available online 2 April 2021

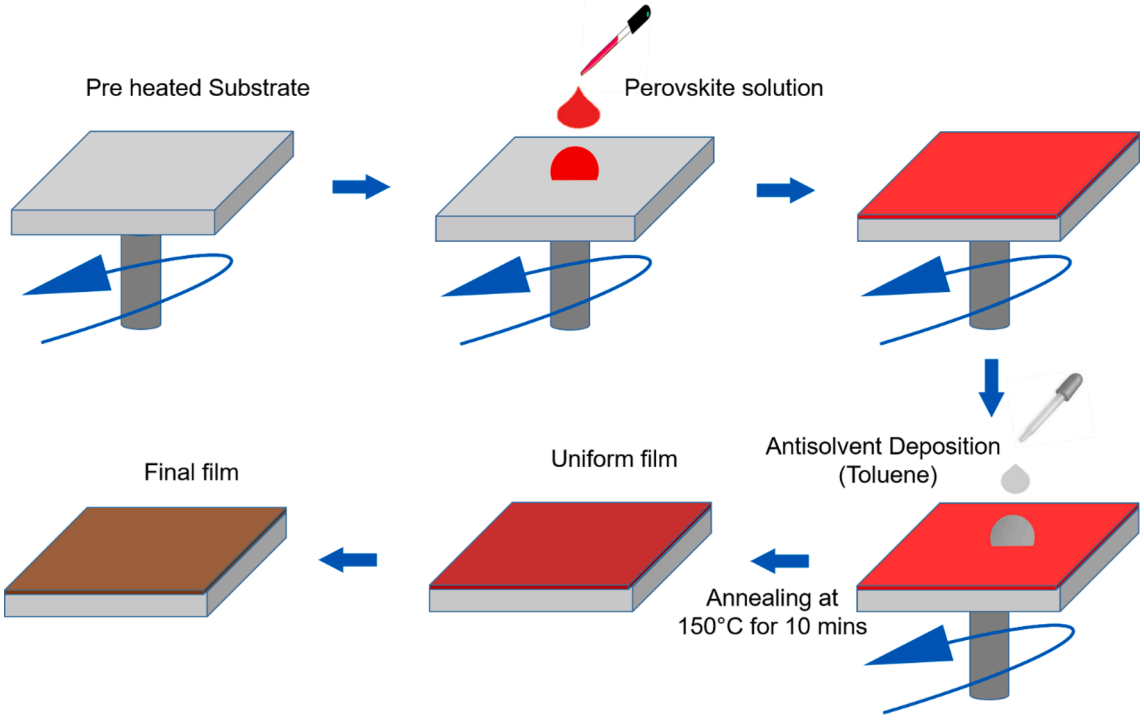

Fig. 1. Schematic representation of single step spin coating process with antisolvent treatment.

structure, whereas δ-phase is a non-perovskite structure. The existence of non-perovskite structure is thermodynamically more stable in ambient atmosphere with high moisture content, whereas the conversion to α-$FAPbI_3$ happens only at temperature above 140 °C (Jeon et al., 2015; Zhou et al., 2016).

In the present work, we explored the doping route in perovskite crystal structure to stabilize the α-$FAPbI_3$ phase and studied the effects of compositional modification on its optical absorbance, band gap, ultrafast fluorescence decay kinetics and the degradation behavior. We doped Bi with Na or K in the B site of $(FA)PbI_3$ perovskite, resulting the stoichiometry of triple cations at B-site i.e. $(FA)K_{0.25}Bi_{0.25}Pb_{0.5}I_3$ or FKBPI and $(FA)Na_{0.25}Bi_{0.25}Pb_{0.5}I_3$ or FNBPI. In order to substitute Pb, researchers engineered various compounds using metals like bismuth, tin etc (Wei et al., 2016; Pazoki et al., 2016; Ran et al., 2017; Wang et al., 2017; Dey et al., 2018; Pazoki et al., 2016; Noel et al., 2014; Jacobsson et al., 2015; Hao et al., 2014; Singh et al., 2016; Eckhardt et al., 2016; Hoye et al., 2016; Sun et al., 2016; Lyu et al., 2016; Park et al., 2015). Albeit, Sn-based perovskite was found to be very hygroscopic (Stoumpos et al., 2013) leading to the formation of SnI_4 as a result of degradation due to moisture. Although the ionic radius of the Bi^{3+} (103 pm) is lower than Pb^{2+} (119 pm) (Shannon, 1976), Bi^{3+} has a lone pair electron similar to Pb^{2+} causing relativistic effect, which stabilizes the perovskite system (Park, 2015). Further, it was reported that incorporation of Na^+ in the perovskite precursor solution (PbI_2) significantly improved the microstructure of planar heterojunction p-i-n solar cell device (Bag and Durstock, 2016). Moreover, the effects of alkali metal ions are well known for CZTS based thin film solar cell (Steinmann et al., 2016; Haass et al., 2018). Low concentration of sodium helps to passivate the non-radiative defects present as well as grain growth (Gershon et al., 2015; Gershon et al., 2015). In the course of searching a lead-free, stable organometallic halide-based PSC, in the current investigation we substituted lead with bismuth in conjugation with alkali metals like sodium and potassium. The replacement of Bi^{3+} seemed difficult to keep the charge neutrality as B site in ABX_3 perovskite is divalent site viz. Pb^{2+} in $MAPbI_3$. Here we selectively chose a cation from Group 1 i.e. Na^+ (or K^+ for FKBPI) and another from Group 15 i.e. Bi^{3+} to make the charge balance. To the best of our knowledge this is the first report on the effect of alkali ions in formamidinium based organic inorganic hybrid solar cell materials. The femtosecond transient absorption technique was used to evaluate ultrafast photoinduced processes occurring in the excited states. The understanding of the charge transfer mechanism within perovskite photo absorber remained poor because the photodynamic parameters of these materials at ultrafast time scale have not been fully investigated till date. In the present article, we focused on the long-term stability, moisture sensitivity and better understanding of charge carrier dynamics of these materials.

2. Experimental section

2.1. Materials

Formamidine acetate (99%), Hydroiodic acid (HI, 57 wt% in H_2O, distilled, stabilized, 99.95%), Lead nitrate ($Pb(NO_3)_2$, 99%), Sodium iodide (NaI, 99.5%), Potassium iodide (KI, 99%) and Bismuth iodide (BiI_3, 99.999%), Titanium(IV) isopropoxide, (99.999%), Fluorine doped tin oxide (FTO) glasses (~13 Ω, TEC15), gold wire (99.99%), anhydrous ɣ-butyrolactone (GBL), absolute ethanol, Toluene (AR) and diethyl ether (Dry, AR) were purchased. All the reagents except toluene were used without any further purification; Toluene was distilled before use.

2.2. Synthesis of formamidinium iodide ($\mathbf{FAI}, \mathbf{H_2NCH = NH_2I}$)

$$H_2NCH = NH \cdot CH_3COOH + HI = H_2NCHNH_2I + CH_3COOH \cdots\cdots \quad (1)$$

FAI was synthesized by reacting HI (33 mL, dropwise) and Formamidine acetate (25 gm) in a 100 mL round bottom flask (RBF) on an ice-water bath with continuous Argon purging and stirring. Temperature was carefully controlled in between 0 and 5 °C. After three hours, the brownish solution was rotary evaporated under vacuum to get viscous brown slurry. Further, it was kept for crystallization. Filtered crystals were washed in diethyl ether. To get extremely pure product, dry crystals were dissolved in warm absolute followed by recrystallized in diethyl ether. Recrystallized product was then dried in vacuum oven at 60 °C for 24 h.

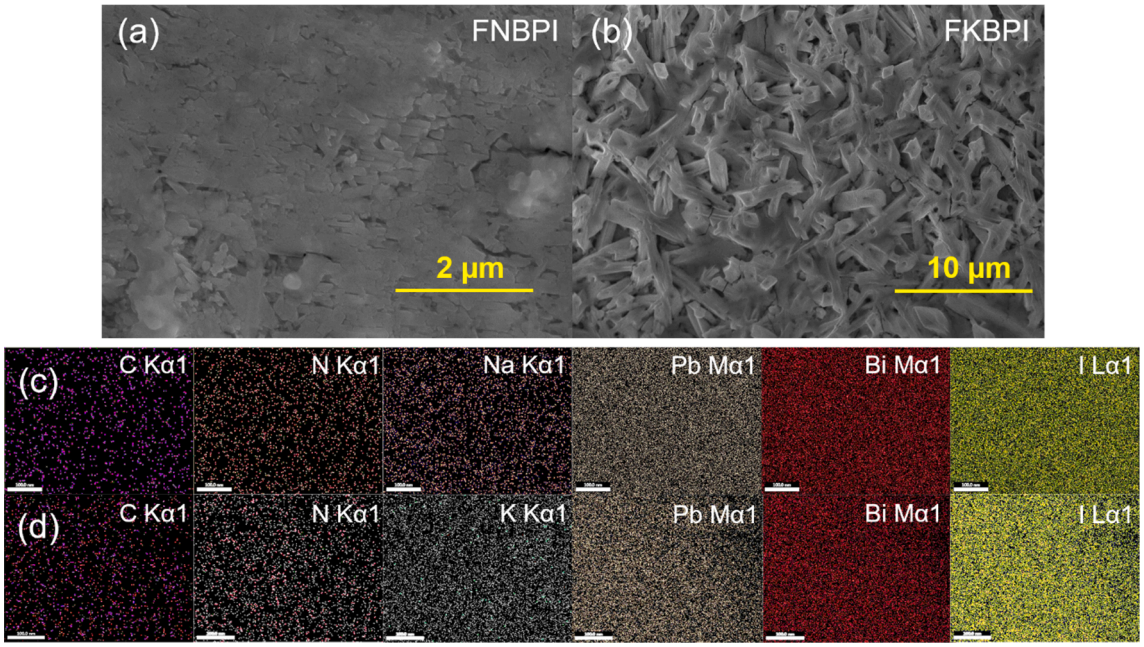

Fig. 2. FESEM microstructural imaging of thin films, (a) FNBPI (b) FKBPI; color mappings of the constituent elements (C, N, Na/K, Pb, Bi and I) in (c) FNBPI and (d) FKBPI obtained by Energy Dispersive X-ray Spectroscopy.

2.3. Lead iodide (PbI_2)

$$Pb(NO_3)_2 + 2KI = PbI_2 + 2KNO_3 \quad (2)$$

lead iodide was synthesized by reacting Lead nitrate and Potassium iodide in 1:2 M ratios in a 500 mL RBF (aqueous medium). Slightly warm KI (aq) was added slowly to Lead nitrate (aq); bright golden crystals of lead iodide were appeared. Filtered crystals were dried in vacuum oven at 80 °C for 6 h.

2.4. Synthesis of perovskite absorbers

Both FKBPI and FNBPI are reddish crystalline powder. FKBPI was synthesized by mixing 4:2:1:1 equivalent molar ratio of formamidinium iodide, lead iodide, bismuth iodide and potassium iodide in GBL in a double neck round bottom flask (RBF).

$$4H_2NCHNH_2I + 2PbI_2 + BiI_3 + KI = 4H_2NCHNH_2(K_{0.25}Bi_{0.25})Pb_{0.5}I_3 \quad (3)$$

$$4H_2NCHNH_2I + 2PbI_2 + BiI_3 + NaI = 4H_2NCHNH_2(Na_{0.25}Bi_{0.25})Pb_{0.5}I_3 \quad (4)$$

The RBF was kept on silicone oil bath for 4 hrs. with continuous stirring and Argon purging; temperature of the solution was maintained at 100 °C. Further, the final product was kept in vacuum oven at 60 °C for 24 h. The synthesis procedure for FNBPI was same as above.

All PSC devices were fabricated on FTO coated glass substrates. To clean the FTO glass substrates, these were ultrasonicated with Hellmanex III soap solution (v/v = 2.5:100 in water) for 30 mins in warm condition followed by ultrasonication in isopropyl alcohol and warm acetone–water mixture respectively for 15 mins in each step. Before deposition, FTO substrates were UV − O_3 treated for 30 mins. The TiO_2 sol precursor of the electron transporting layer (ETL) was prepared by using titanium tetra isopropoxide (TTIP) and ethanol (as solvent) in mild acidic condition. A solution consisting of TTIP and Ethanol (TTIP 500 μL in 5 mL of ethanol with 0.01 M HCl) prepared under the continuous vigorous stirring to get transparent sol. The as-prepared TiO_2 sol was then spin coated on substrate at 4000 rpm for 30 s and subsequently sintered for 500 °C for 1 h with heating rate of 5 °C per minute to form a compact layer. For Perovskite active layer, 0.88 M solution of FKBPI and FNBPI was prepared in GBL for the deposition of thin films. Before deposition of perovskite layer, the solution kept overnight at 55 °C. Spin coating of perovskite precursor was performed on preheated ETL layer on FTO glass substrates at 2500 rpm for 30 s. Further, Toluene was deposited just after 10 s of spin. All the thin film samples were annealed at 100 °C for 10 mins. The schematic of the perovskite active layer film deposition was shown in Fig. 1. Finally, gold was deposited by thermal evaporation as counter electrode with thickness of 50 nm.

2.5. Characterization

X-ray diffraction patterns were collected by PANalytical X'Pert Powder diffractometer with Cu-Kα as incident radiation (λ = 0.154 nm) in the 2θ range between 5° to 55° with step size of 0.01°. All the Field emission scanning electron microscopy (FESEM) images were collected by NOVA NANOSEM 450 machine in secondary electron mode with accelerating voltage of 20 KV. FT-IR experiments were performed in PerkinElmer "Spectrum Two" spectrometer from 450 cm^{-1} to 4000 cm^{-1} of IR radiation. UV–Vis spectroscopy measurement was carried out in the range of 400 nm to 800 nm using Cary 7000 model of Agilent Technologies' UV–Visible spectrophotometer. Fluorescence decays were recorded using a commercial time correlated single photon counting (TCSPC) setup (Life Spec II, Edinburgh Instruments, UK)) with excitation by a 442 nm diode laser (EPL-445, Edinburgh Instruments, UK) and the full width at half maxima of the instrument response function (IRF) was about 120 ps. The time-resolved fluorescence was fitted with sum of three exponentials along with the deconvolution with the IRF. Femtosecond transient absorption measurements were done in a commercial spectrometer (FemtoFrame-II, IB Photonics, Bulgeria). The fundamental 800 nm light was obtained from a Ti:Sapphire regenerative amplifier (Spitfire Pro XP, Spectra-Physics) pumped by a 20 W Q-switched Nd:YLF laser (Empower, Spectra Physics) seeded by a Ti:Sapphire femtosecond oscillator (MaiTai SP, Spectra Physics, USA). In our experimental setup the 800 nm amplifier output had 80 fs pulse duration with 1 kHz repetition rate. One part of the fundamental beam was passed through a β barium borate crystal (BBO) to generate the second harmonic (400 nm), which was used as the pump beam. The power of the pump beam was varied from 15 μW to 30 μW by ND filter for power dependence study. The other part of the fundamental light was passed through a delay stage and then focused on a sapphire crystal to generate white

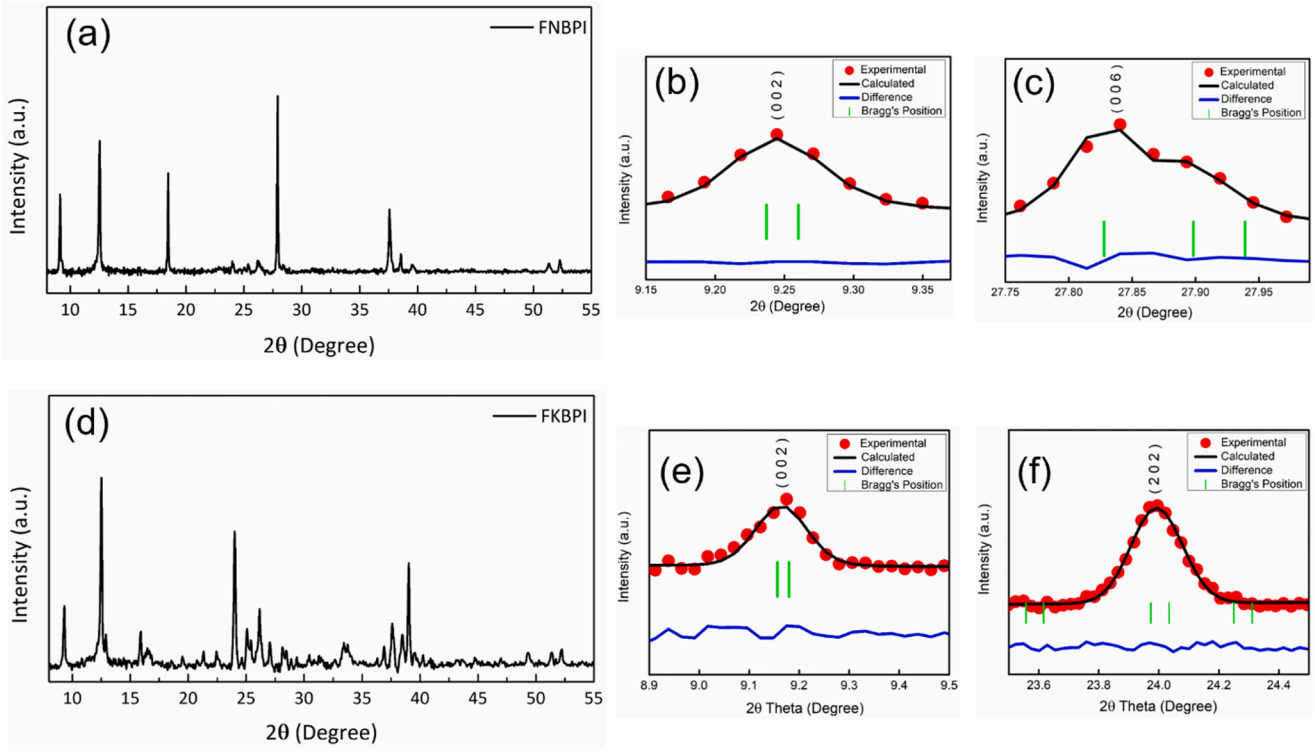

Fig. 3. R.T. X-Ray Diffraction patterns of (a) FNBPI and (d) FKBPI thin films. (b), (c), (e) & (f) Experimental (open circles), calculated (continuous line), difference profile (continuous line) and Bragg position (vertical bars) obtained after LeBail refinement of two single peaks of XRD pattern of respective FNBPI and FKBPI thin films.

light continuum, and this was used as the probe beam. The pump and probe beam were focused onto the sample maintaining the magic angle condition. The probe light was dispersed in a polychromator, and the signal was detected in a CCD. The instrument response function of this set up is 150 fs. The Photovoltaic device characteristics were measured using a Keithley 2400 source meter under dark and simulated solar light (AM1.5G) using a Newport solar simulator.

3. Results and discussion

It is well known that adding antisolvent on top of the wet perovskite film during spin-coating induces fast crystallization (Xiao et al., 2014; Jeon et al., 2014). Antisolvent drop promotes fast nucleation resulting bigger and uniform grains all over the film. Evaporation of solvent during thin film deposition is critical to obtain uniform and homogeneous surface coverage of perovskite films, desirable for an efficient perovskite solar cell (Jeon et al., 2014; Nie et al., 2015). We have chosen toluene as our antisolvent after deciding the perovskite solvent (γ-butyrolactone, GBL). Perovskite precursors are insoluble in toluene but toluene itself is miscible in GBL. Toluene deposition over both FKBPI and FNBPI perovskite films, has removed excess GBL solvent by introducing heterogeneous nucleation. In order to understand the outcome of antisolvent treatment on the perovskite films, morphology of these perovskite thin films has been evaluated by FESEM images as shown in Fig. 2 (a) &(b). Smooth, very uniform, homogeneous mosaic thin film has been observed throughout the FNBPI film after the antisolvent treatment of toluene as evident in Fig. 2(a). On the other hand, ordered 2D perovskite crystals have been found to be uniformly distributed throughout the FKBPI film resulting interlocked microstructure. Although the use of antisolvent has been attributed as the primary reason behind uniform and homogenous films obtained in the present work, it is also plausible that existence of Na^+ or K^+ in these perovskites promotes the formation of larger grains by acting as additional nucleation sites. It is possible that easy diffusion of smaller ions like Na^+ or K^+ facilitates in coalescing multiple grains during the solvent annealing process, resulting in the formation of larger grains. Furthermore, elemental color mappings of FNBPI and FKBPI compositions have been carried out by Energy Dispersive X-ray Spectroscopy to check the distributions of constituents in these perovskites. All the constituents such as C, N, Na/K, Pb, Bi and I have been found to be homogeneously distributed as shown in Fig. 2(c) & (d).

Table 1
Refined structural parameters of FKBPI and FNBPI compositions obtained by LeBail refinement of XRD data using $P4_2/mcm$ space group.

Composition	a = b(Å)	c(Å)	χ^2	R_B
FNBPI	7.128	19.185	4.99	0.89
FKBPI	8.200	19.299	2.30	4.76

The crystal structure has been determined by X-ray diffraction (XRD), performed for as-synthesized thin films of perovskites as shown in Fig. 3(a) & (d) for FNBPI and FKBPI, respectively. Further XRD patterns have been fitted using LeBail method (Le Bail, 2005) with constant scale factor in order to determine the lattice parameter and the space group of the sample as shown in Fig. 3. The fitted data has been found to be consistent with space group $P4_2/mcm$ with tetragonal unit cell ($a = b \neq c, \alpha = \beta = \gamma = 90^{\circ}$) for Both FKBPI and FNBPI. Refined structural parameters of FKBPI and FNBPI compositions obtained by LeBail refinement of XRD data are presented in Table 1. The lattice parameters and unit cell volume of FKBPI have been found to be higher than that of FNBPI. It is expected since K^+ (138 pm) has larger ionic radius compared to that of Na^+ (102 pm).

The compositional engineering provides the freedom to tune the band gap of the material as well. The Na (102 pm) and Bi (103 pm) have comparable ionic radius. However, K has the larger ionic radius (138 pm). Room temperature UV–Vis spectra, shown in Fig. 4(a) have demonstrated high absorption in these perovskites. The absorption

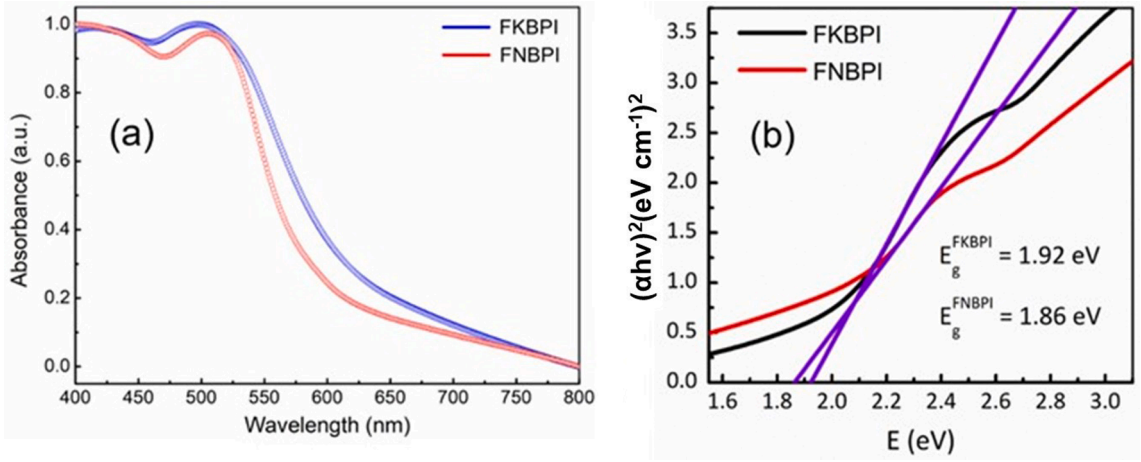

Fig. 4. (a) R.T. UV–Vis absorption spectra with emission, excited by 532 nm laser; (b) estimated optical band gap plot through Tauc equation.

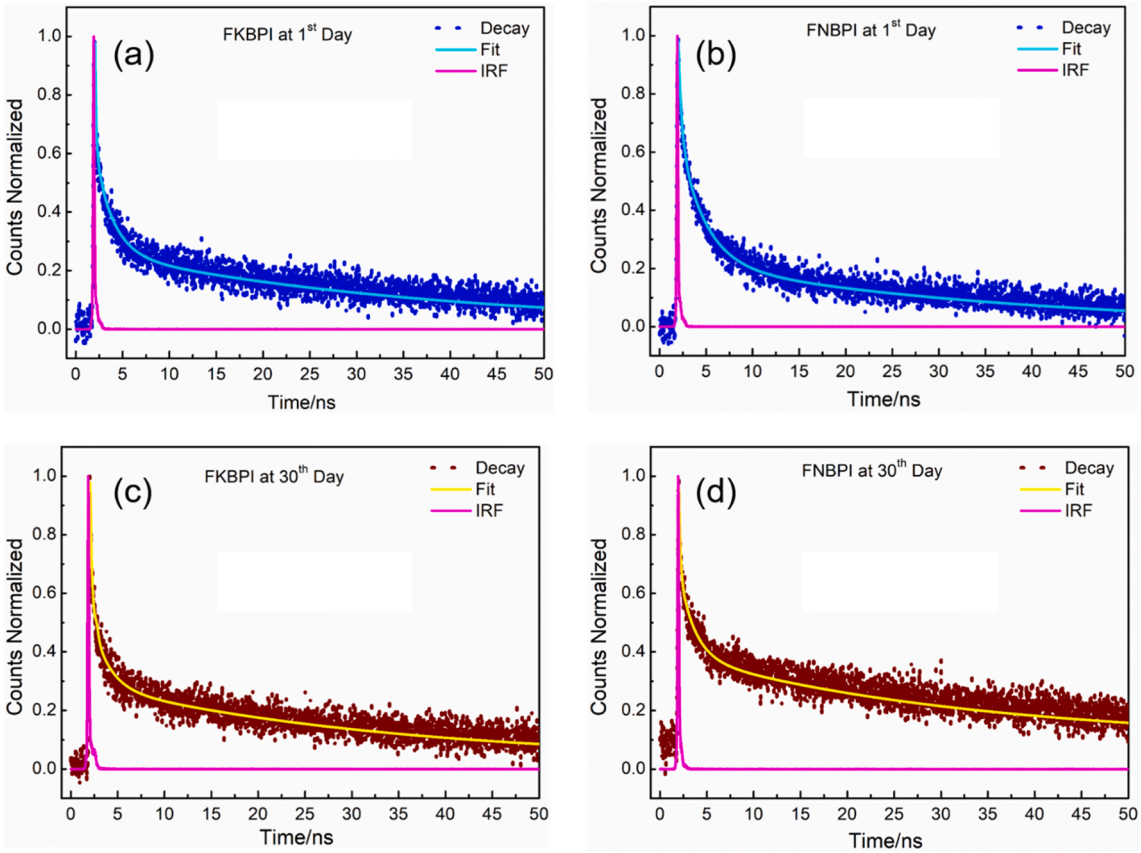

Fig. 5. Fluorescence decay of thin films of (a) FKBPI at Day 1 (b) FNBPI at Day 1 (c) FKBPI at Day 30 and (d) FNBPI at Day 30. λ_{ex} = 442 nm and λ_{em} = 530 nm.

spectra have been recorded from 400 nm to 800 nm. It is evident that both the perovskites have shown excellent absorption up to the 600 nm of visible region of light with high absorption coefficient. Compare to purely lead based perovskite materials, bismuth-based materials absorbed light at the higher energy side of the spectrum which resulted distinct color difference in FNBPI and FKBPI compare to $MAPbI_3$. The estimated absorption coefficient was in the order of 10^5 and the peak absorption occurred at 504 nm. Fig. 4(b) represents Tauc plot. Optical band gap has been calculated by Tauc plot (Tauc, 1968) using Eqn (5).

$$\alpha h\nu = A(h\nu - E_g)^n \quad (5)$$

where, A is a constant, α is absorption coefficient and E_g is the energy gap between HOMO and LUMO; the values of n depend on the mode of transitions; here n = 2 for allowed direct transition. The band gaps (E_g) of FKBPI and FNBPI have been estimated to be 1.92 eV and 1.86 eV respectively. Although, derived band gap energy values of our materials are higher than the band gap energy of $MAPbI_3$ (1.55 eV) (Park, 2015). The achieved E_g is much lower than the other reported bi-based halide perovskites. The reported bandgap of methylammonium based double perovskite, $(MA)_2KBiCl_6$ is 3.04 eV (Wei et al., 2016). $Cs_2AgBiBr_6$ and $Cs_2AgBiCl_6$ exhibit bandgap of 2.26 eV and 3.0 eV respectively (McClure et al., 2016). There is an another report corresponding to the bandgap of $Cs_2AgBiBr_6$, Where E_g is 1.95 eV (Slavney et al., 2016). However, the lowest reported bandgap has been 1.86 eV for $Cs_2Ag(Bi_{0.625}Sb_{0.375})Br_6$

Table 2
Lifetime component analysis of FKBPI and FNBPI thin film.

Sample	Day	τ_1 in ns (%)	τ_2 in ns (%)	τ_3 in ns (%)
FKBPI	Day 1	0.2 (67%)	3.6 (12%)	21 (21%)
	Day 30	0.2 (71%)	3.3 (10%)	23 (19%)
FNBPI	Day1	0.2 (58%)	2.9 (20%)	26 (22%)
	Day 30	0.2 (52%)	3.1 (16%)	22 (32%)

composition (Du et al., 2017). Although the energy difference between HOMO and LUMO is as high as 3.3 eV, $Cs_2InAgCl_6$ double perovskite shows direct transition (Volonakis et al., 2017).

Furthermore, we explored the ultrafast dynamics of both the perovskites by ultrafast optical spectroscopy techniques. The time correlated single photon counting (TCSPC) and femtosecond transient absorption techniques have enabled us to evaluate ultrafast photoinduced processes occurring in the perovskite materials under investigation. The understanding of fundamental photophysical dynamics of these materials is very important to evaluate the potential of new perovskites for solar cell application.

Fig. 5 depicts the fluorescence transients of FNBPI and FKBPI films, deposited on FTO glass without any ETL . Room temperature photoluminescence spectra of the samples are shown in Fig. S1 of the SI. To determine the relative concentrations of the extracted and recombined charge carriers and their respective lifetimes, the fluorescence transients have been fitted to tri-exponential function along with the deconvolution with the IRF by iterative re-convolution method. The fitting lines are shown in Fig. 5 and the fitting parameters are tabulated in Table 2. The most exciting thing about these perovskites is their 30th day carrier lifetimes measured after keeping both the films in ambient atmosphere for one month. They have demonstrated remarkable moisture resistance behavior.

The sub nanosecond component of 0.2 ns in both FKBPI and FNBPI is a quenching component, mainly arising due to the formation of deep traps upon bismuth incorporation within the crystal (Yin et al., 2019; Harikesh et al., 2018). The lifetime component around 3 ns is assigned for the excitonic recombination (Begum et al., 2017; Yang et al., 2017; Peng et al., 2017) while the long component over 25 ns is the result of carrier recombination via the surface trapping sites (Begum et al., 2017; Yang et al., 2017). The formation of deep traps within the crystal upon

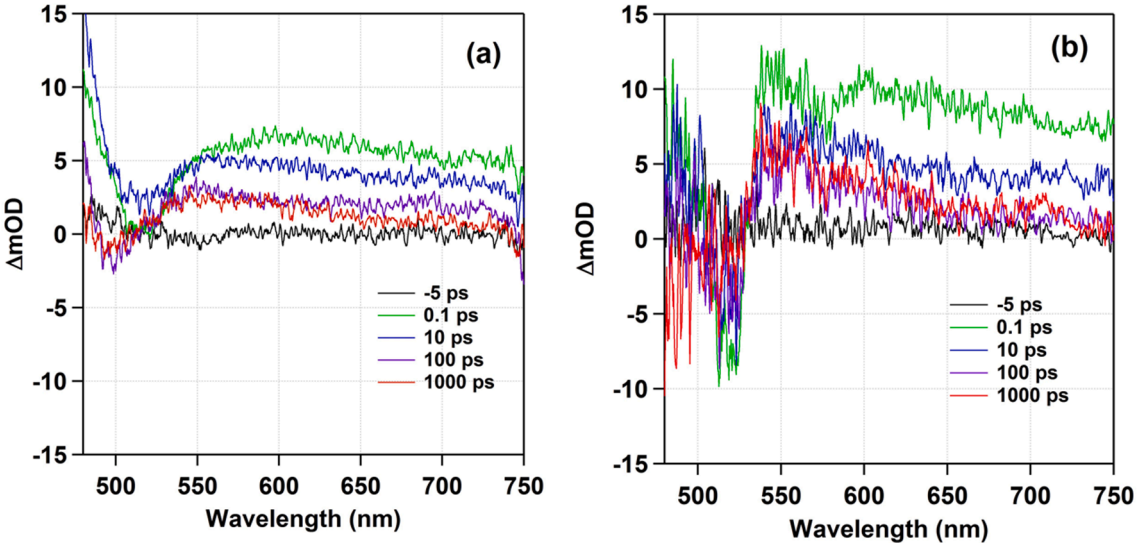

Fig. 6. Femtosecond transient absorption spectra of (a) FNBPI and (b) FKBPI. Pump wavelength is 400 nm and the pump power are 25 μW.

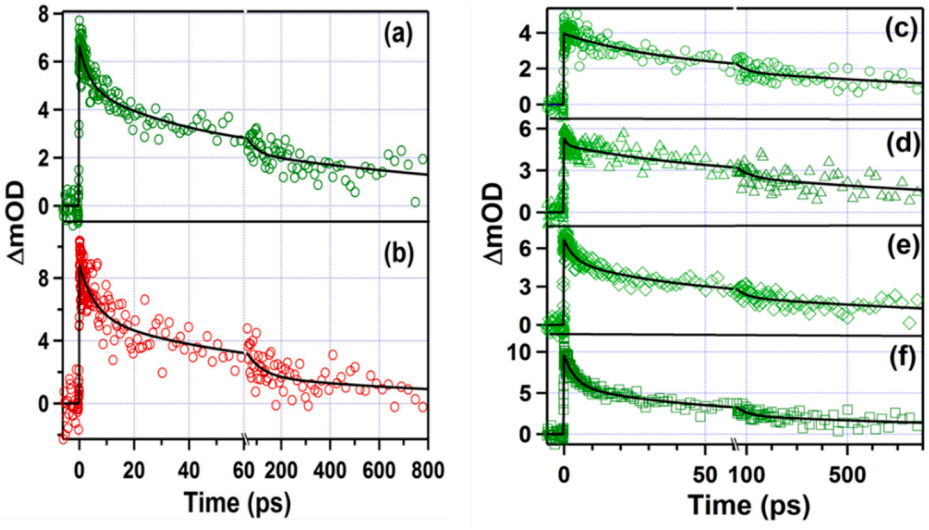

Fig. 7. Decay kinetics of (a) FNBPI and (b) FKBPI at probe 620 nm and pump power 25 μW. Decay kinetics of FNBPI at pump power (c) 15 μW, (d) 20 μW, (e) 25 μW and (f) 30 μW.

Table 3
Fitting parameters of TA kinetics at 620 nm of FNBPI and FKBPI. Contributions of the processes are given in parenthesis.

Sample	Power of Pump (μW)	τ_1 in ps (%)	τ_2 in ps (%)	τ_3 in ps (%)
FNBPI	15	0.3 (1%)	41 (52%)	1746 (47%)
	20	1.1 (11%)	54 (41%)	1644 (48%)
	25	3.7 (25%)	42 (41%)	1445 (34%)
	30	4.1 (40%)	49 (36%)	1565 (24%)
FKBPI	25	5.9 (37%)	65 (42%)	1176 (21%)

bismuth insertion originates because of inertness of the 6 s orbital of the bismuth that leads to weak interaction with the halide ions (Harikesh et al., 2018). These deep traps restrict the charge carrier mobility and affects the solar cell performance. In the present investigation, this quenching component arising because of charge carrier trapping within the deep traps has been found to persist in both FKBPI and FNBPI. The relative contribution of trapping transfer process in FKBPI is higher than in FNBPI. Relatively lower contribution of trapping process in FNBPI than FKBPI also indicates the possibility of favorable passivation of deep traps by sodium than potassium which makes FNBPI superior candidate for solar cell. However, the interaction of potassium and sodium with the deep traps within the lattice needs further studies. To check the stability issue, time resolved studies have been carried out for both FKBPI and FNBPI, which shows almost unaltered average lifetime, and confirms that both the thin films are stable in open atmosphere.

To gain a better understanding of the sub-nanosecond carrier dynamics femtosecond transient absorption studies for both FKBPI and FNBPI have been performed, which are depicted in Fig. 6. A broad photo induced absorption (PIA) around 520 to 750 nm has been observed for both the samples upon excitation at 400 nm (25 μW pump power). Furthermore, 620 nm transients of FNBPI and FKBPI thin films have been collected with 25 μW pump power, which have been found to be best fitted with a three-exponential function as shown in Fig. 7 and the fitting results are tabulated in table 3. The short time component of few ps has been assigned to the auger recombination process (Li et al., 2020). It has been anticipated that 50 ps time component is due to the trapping of charged carrier by the deep trapping site within the lattice and further longer time component has been attributed to the free charge carrier recombination (Begum et al., 2017; Sum et al., 2016; Sheng et al., 2015; Deng et al., 2016). As the time window of our measurement is 1800 ps, we could not be accurate for the exact time constant beyond that. It is also evident from Table 3 that the third lifetime component decreases significantly from FNBPI (1445 ps, 34%)) to FKBPI (1176 ps, 21%), which signifies that the free electron-hole recombination process become much faster. This also indicates that FNBPI thin film should be superior as a solar cell material than FKBPI thin film.

Moreover, we performed a pump power dependence measurement of FNBPI dynamics to have a better understanding of the various recombination processes. Usually at low carrier density, the auger process (which are not unimolecular) are expected to contribute less in the overall relaxation process and under a high pump power, the carrier density is expected to increase (Sum et al., 2016; Sheng et al., 2015; Deng et al., 2016; Piatkowski et al., 2015). Our pump power dependence study has further validated this, where the contribution of the fast decay component was seen to increase from 1% to 40% by increasing the pump power from 15 μW to 30 μW, as depicted in Fig. 7c to 7f. Furthermore, there are no noticeable change in the TA spectra at the higher pump powers with a broad PIA around 520 nm to 750 nm as shown in Fig. S2. On the other hand, the slow component is found to be inversely proportional to the pump power, which confirms that its origin is free electron-hole recombination process as favourable higher-molecular recombination process results in decrease in the contribution of the free electron hole recombination.

3.1. Device characterization

Optical properties and the morphology of the photo absorber material are the two important key factor that determines the efficiency of thin film based perovskite solar cells. To determine the photovoltaic properties of tetra cation based perovskite active layer, we have fabricated the device with conventional n-i-p configuration as also shown in Fig. 8. The current density-Voltage (J-V) measurements of both the potassium and sodium based formamidinium solar cells are shown in Fig. 9. All the photovoltaic parameters such as V_{oc}, J_{SC}, FF, and η of all the devices measured are listed in the Table S1 in Supporting Information. The photovoltaic parameters of the best performance device of FNBPI perovskite are determined as FF = 0.35, V_{oc} = 0. 35, J_{SC} = 4.23 mAcm^{-2} and η = 0.52%; whereas that for FKBPI are measured as FF = 0.37, V_{oc} =

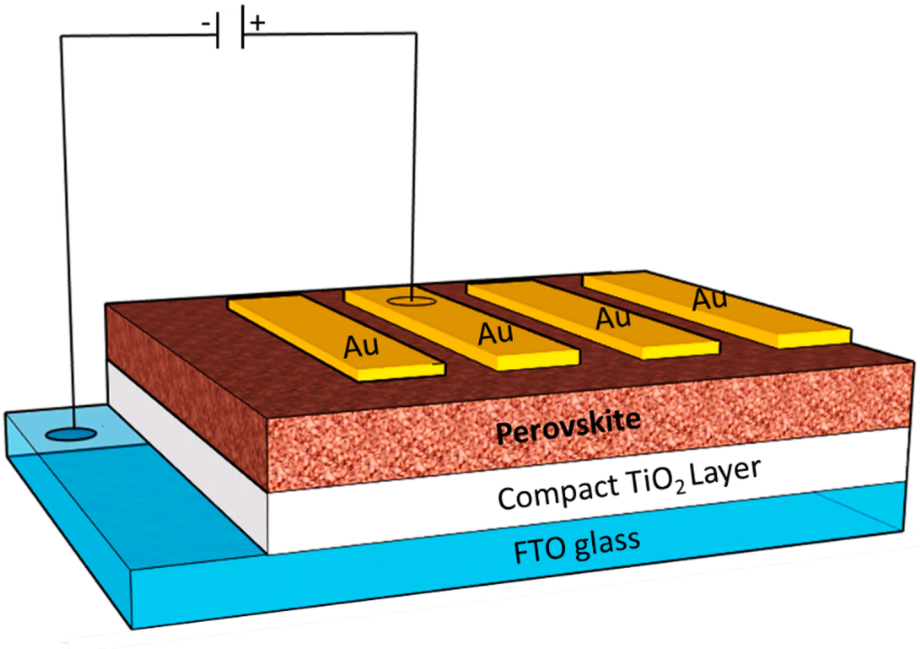

Fig. 8. Schematic device architecture of fabricated solar cell device.

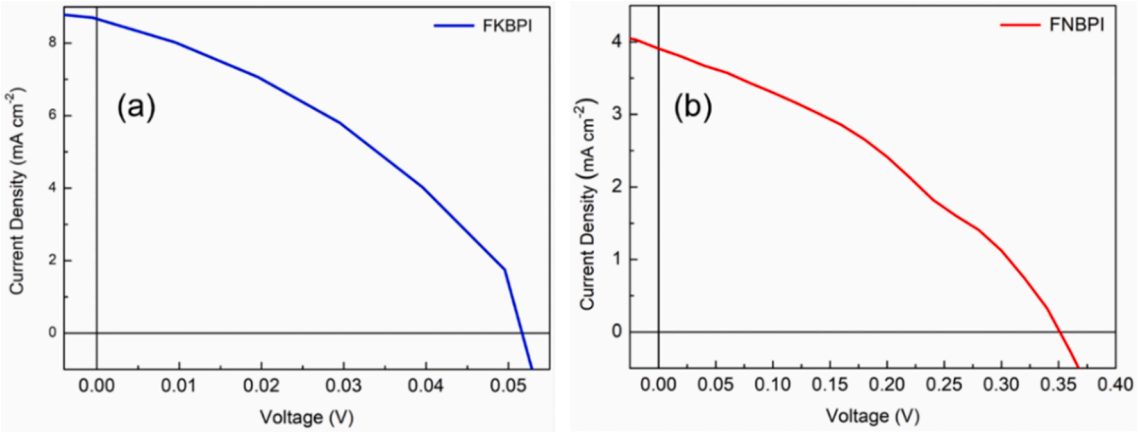

Fig. 9. J-V curve of FNBPI under reverse bias condition.

Table 4
Comparison of the Bi-based PSCs with other devices reported in the literature.

Sl. No.	Device architecture	Processing Method	V_{OC} (V)	J_{SC} (mA/cm^2)	FF	PCE (%)	Ref No. (Year)
1.	FTO/TiO_2/*meso*-TiO_2/ $(FA)_3Bi_2I_9$ /spiroMeOTAD/Au	Spin-coating	0.45	0.11	0.459	0.022	(Lan et al., 2019) (2019)
2.	FTO/ *meso*-TiO_2/ $(MA)_3Bi_2I_9$/ spiroMeOTAD/Au	Chemical Vapor Deposition	0.40	0.11	0.36	0.016	(Sanders et al., 2018) (2019)
3.	FTO/TiO_2/*meso*-TiO_2/ $(MA)_3Bi_2I_9$/P3HT /Ag	Spray deposition	0.214	2.33	0.33	0.17	(Mohammad et al., 2019) (2019)
4.	FTO/TiO_2/*meso*-TiO_2/ $(MA)_3Bi_2I_9$/P3HT /Ag	Spin-coating	0.588	1.18	0.48	0.33	(Li et al., 2019) (2019)
5.	FTO/TiO_2/*meso*-TiO_2/ $(MA)_3Bi_2I_9$/spiroMeOTAD/Ag	Spin-coating	0.68	0.52	0.33	0.12	(Park et al., 2015) (2015)
6.	ITO/TiO_2/ $(MA)_3Bi_2I_9$/ spiro-MeOTAD/Au	Spin-coating	0.72	0.49	0.32	0.11	(Abulikemu et al., 2016) (2016)
7.	FTO/TiO_2/*meso*-TiO_2/ $(MA)_3Bi_2I_9$/P3HT/Au	Spin-coating	0.35	1.16	0.46	0.19	(Lyu et al., 2016) (2016)
8.	FTO/ Anatase/*meso*-TiO_2/ $(MA)_3Bi_2I_9$/spiroMeOTAD/Au	Spin-coating	0.56	0.83	0.48	0.26	(Singh et al., 2016) (2016)
9.	ITO/PEDOT:PSS/ /$(MA)_3Bi_2I_9$/C60/BCP/Ag	Evaporation	0.83	1.39	0.34	0.39	(Ran et al., 2017) (2017)
10.	FTO/ TiO_2/*meso*-TiO_2/ $(MA)_3Bi_2I_9$/spiroMeOTAD/Au	Spin-coating	0.87	1.6	0.34	0.41	(Ahmad et al., 2019) (2019)
11.	ITO/ TiO_2/*meso*-TiO_2/ $(MA)_3Bi_2I_9$/spiro-MeOTAD/ MoO_3/Ag	Spin-coating	0.67	1.00	0.62	0.42	(Zhang et al., 2016) (2016)
12.	FTO/ TiO_2/*meso*-TiO_2/ $(MA)_3Bi_2I_9$/spiroMeOTAD/Au	Vacuum deposition	0.83	3.00	0.79	1.64	(Zhang et al., 2017) (2017)
13.	FTO/TiO_2/*meso*-TiO_2/ $(MA)_3Bi_2I_9$/P3HT /Au	vapour assisted solution process	1.01	4.02	0.78	3.17	(Jain et al., 2018) (2018)
14.	FTO/ TiO_2/*meso*-TiO_2/ FNBPI /Au	Spin-coating	0.35	4.23	0.35	0.52	Current Work

0.05, $J_{SC} = 8.68\ mAcm^{-2}$ and $\eta = 0.16\%$. The higher J_{SC} values of FNBPI compared to FKBPI absorber layers corroborate well with our observation of faster recombination process of FKBPI compared to FNBPI in transient absorption kinetics study as discussed above. Also the FNBPI active layer shows more compact morphology (Fig. 2) due to addition of sodium at B site of the perovskite, which also helped in ameliorating the device efficiency by three times as compared to the FKBPI based device.

Further we compare our device performance with Bi-based PSC reported in the literature as shown in Table 4. It can be seen that maximum efficiency of 0.52% obtained in our spin-coated FNBPI device is slightly higher that other reported in the literature. However, vapor-assisted, or vacuum deposited samples exhibit better efficiency. The primary reasons for the low efficiency of our as fabricated device are due to the low open circuit voltages as well as low fill factor. We anticipated that further study for the proper selection of ETM and HTM can improve PCE. The tail of the absorption spectrum suggests the presence of more band gap states of these Bi based perovskites compare to only Pb based perovskites. This increased number of band gap states may contribute to the various recombination pathways which therefore leads to low photocurrent and photovoltage (Park et al., 2015). Moreover, the solar cell performance does not solely depend on the material. For an efficient charge extraction, there should be no recombination at the interfaces of ETM/Active layer what we are using here as ETM is compact layer TiO_2 may not be the best candidate for our materials. The device efficiency can also improve by selection of deposition method of perovskite active layer. Jain et al. have opted vapor-assisted preparation method for $(MA)_3Bi_2I_9$, that shows the device efficiency of 3.17% (Jain et al., 2018). But the efficiencies of most of the bismuth based solar cells remain below 1% (Lyu et al., 2016; Lan et al., 2019; Sanders et al., 2018; Mohammad et al., 2019; Li et al., 2019; Abulikemu et al., 2016; Singh et al., 2016; Ahmad et al., 2019; Zhang et al., 2016; Zhang et al., 2017). Nevertheless, high photo current (4.23 mA/cm^2) obtained in FNBPI shows its potential for developing advanced photodetector.

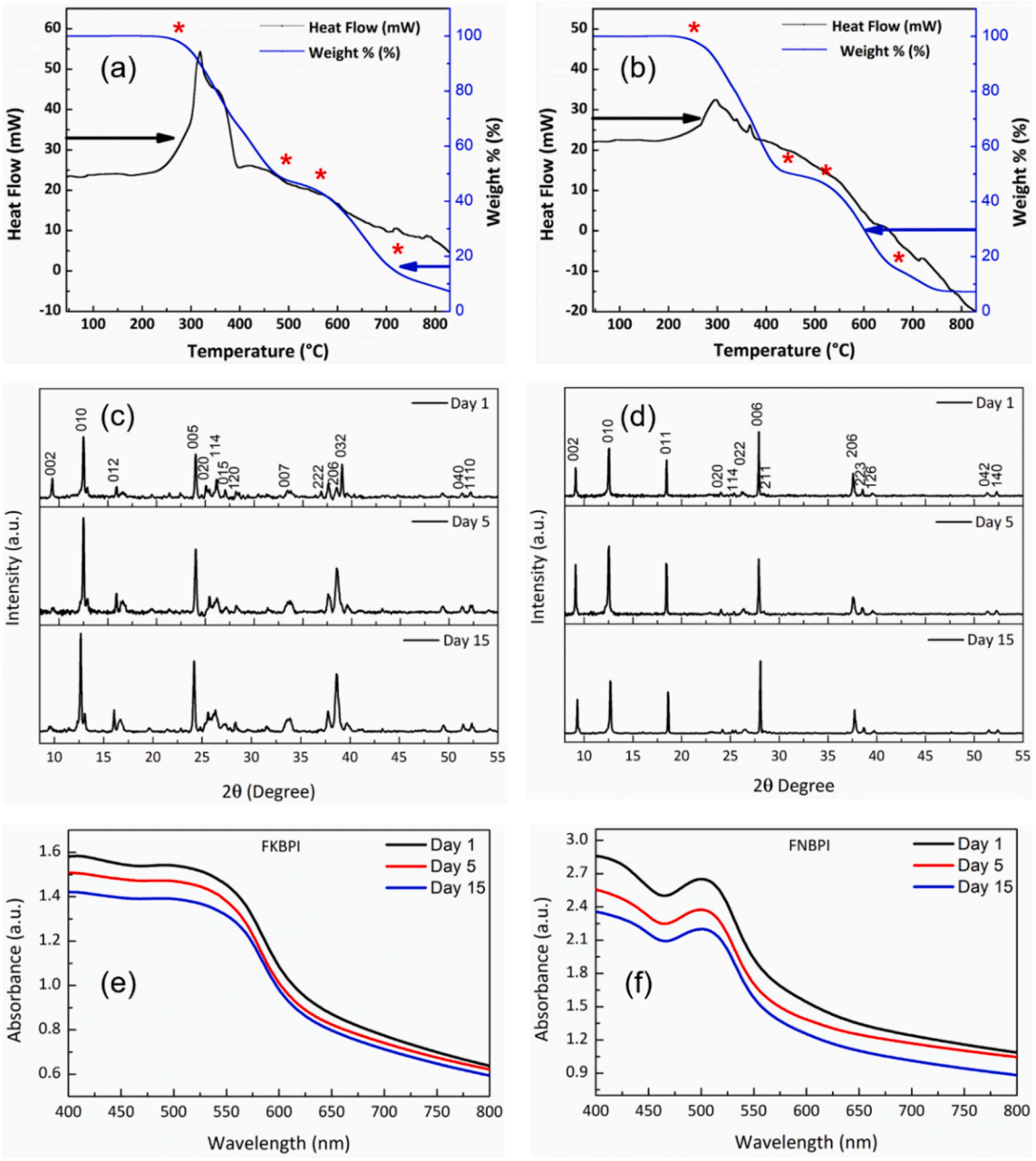

Fig. 10. TGA-DSC analysis curve of (a) FKBPI powder and (b) FNBPI powder heated up to 850 °C. R.T. X-Ray diffraction patterns of (c) FKBPI and (d) FNBPI thin films collected at different time periods. R.T. UV–Vis spectra collected over prolonged period for as synthesized thin film samples of (e) FKBPI and (f) FNBPI.

3.2. Degradation study

We have further recorded the degradation behavior of the perovskite films kept in the ambient condition by using TGA-DSC study, X-ray diffraction patterns and UV–Vis absorption spectra as shown in Fig. 10. The differential scanning calorimetry (DSC) and thermogravimetric analysis (TGA) were performed simultaneously in the temperature range from room temperature to 850 °C to evaluate thermal stability of these perovskites as depicted in Fig. 10 (a) & (b).

TGA graph shows rapid decrease in weight from 270 °C and 290 °C in FNBPI and FKBPI respectively. It is expected since melting point of FAI is 242 °C. At around 500–550 °C almost 75% weight loss has been observed mainly due to PbI_2 and BiI_3 (BP. 542 °C) as their melting point lies at 402 °C and 408.5 °C, respectively. And 90% weight loss has been found to be occurred at around 700 °C because of sodium iodide (MP. 661 °C) and potassium iodide (MP. 681 °C). TGA plot suggests that there has been less than 1% decomposition in the temperature range up to 233 °C and 252 °C in FNBPI and FKBPI, respectively. Similarly, almost no change has been observed in the DSC curve until 220 °C and 230 °C in FNBPI & FKBPI respectively. TGA-DSC studies suggests that both the perovskite materials are stable up to 230 °C at least. In order to evaluate stability of the perovskite films in ambient condition, same thin film samples have been used for characterization throughout the experiments. However, there is no notable sign of degradation even after 15th day in the XRD profile of both perovskites as illustrated in Fig. 10(c) & (d), suggesting superior resistance to moisture compare to its predecessors. Furthermore, UV–visible spectra have demonstrated that not much changes in their respective absorption spectra except certain decrease in the overall absorption coefficient. Both these perovskites have exhibited strong optical absorption even after two weeks as stated in Fig. 10(e) & (f). The superior moisture resistance can be attributed to the high relativistic effect of bismuth. Due to relativistic effect, the s

orbital electrons are forced to become closer to the nucleus while the d and f orbital electrons are moved away. As a result, oxidation resistance increases for the element having relativistic effect (Bartlett, 1998), which is the consequence of high atomic number (Z) elements. Sn (Z = 50) experiences less relativistic effect compare to Pb (Z = 82). That's why Sn gets readily oxidized into Sn^{+4}. On the contrary, due to the large relativistic effect of Bi (Z = 83), it can be considered as a potential replacement of Pb in the PSC with better stability.

4. Conclusions

In summary, we have synthesized highly crystalline $NH_2CHNH_2(K_{0.25}Bi_{0.25})Pb_{0.5}I_3$ aka. FKBPI and $NH_2CHNH_2(Na_{0.25}Bi_{0.25})Pb_{0.5}I_3$ aka. FNBPI perovskites with tetragonal crystal structure. UV–Vis spectra revealed high absorption in these perovskites with estimated band gap of 1.92 eV and 1.86 eV for FKBPI and FNBPI, respectively. Further, we studied a detailed photophysical processes in FNBPI and FKBPI thin films through TCSPC and f-TAS techniques. Average charge carrier lifetimes are estimated as 1.92 ns and 3.99 ns for FKBPI and FNBPI thin films, respectively even after keeping these perovskites at ambient atmosphere for 30 days. Our periodical XRD pattern and UV–Vis spectra have confirmed better moisture stability for these perovskite thin films due to bismuth incorporation. Better energy conversion efficiency obtained in FNBPI based solar cell compared to FKBPI has been further explained using femtosecond transient absorption study, which implies faster free electron-hole recombination process in perovskite having potassium compared to sodium. Although provisionally we have achieved highest PCE 0.52% in FNBPI, further work on selection of ETM and use of HTM is necessary to enhance its efficiency.

Declaration of Competing Interest

The authors declare that they have no known competing financial interests or personal relationships that could have appeared to influence the work reported in this paper.

Acknowledgement

Authors acknowledge the kind help of Prof. S. S. K. Iyer, Department of Electrical Engineering, IITK and National Centre for Flexible Electronics in measurement of the solar cell efficiency.

Appendix A. Supplementary data

Supplementary data to this article can be found online at https://doi.org/10.1016/j.solener.2021.03.031.

References

Abulikemu, M., Ould-Chikh, S., Miao, X., Alarousu, E., Murali, B., Ngongang Ndjawa, G. O., Barbé, J., El Labban, A., Amassian, A., Del Gobbo, S., 2016. Optoelectronic and Photovoltaic Properties of the Air-Stable Organohalide Semiconductor $(CH_3NH_3)_3Bi_2I_9$. J. Mater. Chem. A 4 (32), 12504–12515.

Ahmad, K., Ansari, S.N., Natarajan, K., Mobin, S.M., 2019. A $(CH_3NH_3)_3Bi_2I_9$. Perovskite Based on a Two-Step Deposition Method: Lead-Free, Highly Stable, and with Enhanced Photovoltaic Performance. ChemElectroChem 6 (4), 1192–1198.

Bag, S., Durstock, M.F., 2016. Large Perovskite Grain Growth in Low-Temperature Solution-Processed Planar p-i-n Solar Cells by Sodium Addition. ACS Appl. Mater. Interfaces 8 (8), 5053–5057.

Ball, J.M., Lee, M.M., Hey, A., Snaith, H.J., 2013. Low-Temperature Processed Meso-Superstructured to Thin-Film Perovskite Solar Cells. Energy Environmen. Sci. 6, 1739–1743.

Bartlett, N., 1998. Relativistic Effects and the Chemistry of Gold. Gold Bull. 31 (1), 22–25.

Begum, R., Parida, M.R., Abdelhady, A.L., Murali, B., Alyami, N.M., Ahmed, G.H., Hedhili, M.N., Bakr, O.M., Mohammed, O.F., 2017. Engineering Interfacial Charge Transfer in $CsPbBr_3$ Perovskite Nanocrystals by Heterovalent Doping. J. Am. Chem. Soc. 139 (2), 731–737.

Burschka, J., Pellet, N., Moon, S.-J., Humphry-Baker, R., Gao, P., Nazeeruddin, M.K., Grätzel, M., 2013. Sequential Deposition as a Route to High-Performance Perovskite-Sensitized Solar Cells. Nature 499, 316–319.

Comin, R., Walters, G., Thibau, E.S., Voznyy, O., Lu, Z.H., Sargent, E.H., 2015. Structural, Optical, and Electronic Studies of Wide-Bandgap Lead Halide Perovskites. J. Mater. Chem. C 3 (34), 8839–8843.

Deng, X., Wen, X., Huang, S., Sheng, R., Harada, T., Kee, T.W., Green, M., Ho-Baillie, A., 2016. Ultrafast Carrier Dynamics in Methylammonium Lead Bromide Perovskite. J. Phys. Chem. C 120 (5), 2542–2547.

Dey, P., Khorwal, V., Sen, P., Biswas, K., Maiti, T., 2018. Spectral Studies of Lead-Free Organic-Inorganic Hybrid Solid-State Perovskites $CH_3NH_3Bi_{2/3}I_3$ and $CH_3NH_3Pb_{1/2}Bi_{1/3}I_3$: Potential Photo Absorbers. ChemistrySelect 3 (2), 794–800.

Du, K.Z., Meng, W., Wang, X., Yan, Y., Mitzi, D.B., 2017. Bandgap Engineering of Lead-Free Double Perovskite $Cs_2AgBiBr_6$ through Trivalent Metal Alloying. Angew. Chemie - Int. Ed. 56 (28), 8158–8162.

Eckhardt, K., Bon, V., Getzschmann, J., Grothe, J., Wisser, F.M., Kaskel, S., 2016. Crystallographic Insights into $(CH_3NH_3)_3(Bi_2I_9)$: A New Lead-Free Hybrid Organic-Inorganic Material as a Potential Absorber for Photovoltaics. Chem. Commun. 52, 3058–3060.

Fang, H.H., Wang, F., Adjokatse, S., Zhao, N., Even, J., Loi, M.A., 2016. Photoexcitation Dynamics in Solution-Processed Formamidinium Lead Iodide Perovskite Thin Films for Solar Cell Applications. Light Sci. Appl. 5 (4), e16056.

Gershon, B.T., Lee, Y.S., Mankad, R., Gunawan, O., Gokmen, T., Bishop, D., McCandless, B., Guha, S., 2015. The Impact of Sodium on the Sub-Bandgap States in CZTSe and CZTS. Appl. Phys. Lett. 106 (12), 123905.

Gershon, T., Shin, B., Bojarczuk, N., Hopstaken, M., Mitzi, D.B., Guha, S., 2015. The Role of Sodium as a Surfactant and Suppressor of Non-Radiative Recombination at Internal Surfaces in Cu_2ZnSnS_4. Adv. Energy Mater. 5 (2), 1400849.

Grätzel, M., 2014. The Light and Shade of Perovskite Solar Cells. Nat. Mater. 13, 838–842.

Green, M., Ho-Baillie, A., Snaith, H., 2014. The emergence of perovskite solar cells. Nat. Photon 8, 506–514.

Haass, S.G., Andres, C., Figi, R., Schreiner, C., Bürki, M., Romanyuk, Y.E., Tiwari, A.N., 2018. Complex Interplay between Absorber Composition and Alkali Doping in High-Efficiency Kesterite Solar Cells. Adv. Energy Mater. 8 (4), 1701760.

Habisreutinger, S.N., Leijtens, T., Eperon, G.E., Stranks, S.D., Nicholas, R.J., Snaith, H.J., 2014. Carbon Nanotube/Polymer Composites as a Highly Stable Hole Collection Layer in Perovskite Solar Cells. Nano Lett. 14 (10), 5561–5568.

Han, Q., Bae, S.H., Sun, P., Hsieh, Y.T., Yang, Y., Rim, Y.S., Zhao, H., Chen, Q., Shi, W., Li, G., Yeng, Y., 2016. Single Crystal Formamidinium Lead Iodide $(FAPbI_3)$: Insight into the Structural, Optical, and Electrical Properties. Adv. Mater. 28 (11), 2253–2258.

Hao, F., Stoumpos, C.C., Cao, D.H., Chang, R.P.H., Kanatzidis, M.G., 2014. Lead-Free Solid-State Organic-Inorganic Halide Perovskite Solar Cells. Nat. Photon. 8 (6), 489–494.

Harikesh, P.C., Wu, B., Ghosh, B., John, R.A., Lie, S., Thirumal, K., Wong, L.H., Sum, T.C., Mhaisalkar, S., Mathews, N., 2018. Doping and Switchable Photovoltaic Effect in Lead-Free Perovskites Enabled by Metal Cation Transmutation. Adv. Mater. 30 (34), 1802080.

Hoye, R.L.Z., Brandt, R.E., Osherov, A., Stevanović, V., Stranks, S.D., Wilson, M.W.B., Kim, H., Akey, A.J., Perkins, J.D., Kurchin, R.C., Poindexter, J.R., Wang, E.N., Bawendi, M.G., Bulović, V., Buonassisi, T., 2016. Methylammonium Bismuth Iodide as a Lead-Free, Stable Hybrid Organic-Inorganic Solar Absorber. Chem. - A Eur. J. 22 (8), 2605–2610.

Jacobsson, T.J., Pazoki, M., Hagfeldt, A., Edvinsson, T., 2015. Goldschmidt Rules and Strontium Replacement in Lead Halogen Perovskite Solar Cells: Theory and Preliminary Experiments on $CH_3NH_3SrI_3$. J. Phys. Chem. C 119 (46), 25673–25683.

Jain, S.M., Phuyal, D., Davies, M.L., Li, M., Philippe, B., De Castro, C., Qiu, Z., Kim, J., Watson, T., Tsoi, W.C., Karis, O., Rensmo, H., Boschloo, G., Edvinsson, T., Durrant, J. R., 2018. An Effective Approach of Vapour Assisted Morphological Tailoring for Reducing Metal Defect Sites in Lead-Free, $(CH_3NH_3)_3Bi_2I_9$ Bismuth-Based Perovskite Solar Cells for Improved Performance and Long-Term Stability. Nano Energy 49, 614–624.

Jeon, N.J., Noh, J.H., Kim, Y.C., Yang, W.S., Ryu, S., Seok, S.I., 2014. Solvent Engineering for High-Performance Inorganic-Organic Hybrid Perovskite Solar Cells. Nat. Mater. 13 (9), 897–903.

Jeon, N.J., Noh, J.H., Yang, W.S., Kim, Y.C., Ryu, S., Seo, J., Seok, S.I., 2015. Compositional Engineering of Perovskite Materials for High-Performance Solar Cells. Nature 517 (7535), 476–480.

Jiang, Y., Juarez-Perez, E.J., Ge, Q., Wang, S., Leyden, M.R., Ono, L.K., Raga, S.R., Hu, J., Qi, Y., 2016. Post-Annealing of $MAPbI_3$ Perovskite Films with Methylamine for Efficient Perovskite Solar Cells. Mater. Horiz. 3, 548–555.

Kojima, A., Teshima, K., Shirai, Y., Miyasaka, T., 2009. Organometal Halide Perovskites as Visible-Light Sensitizers for Photovoltaic Cells. J. Am. Chem. Soc. 131 (17), 6050–6051.

Lan, C., Liang, G., Zhao, S., Lan, H., Peng, H., Zhang, D., Sun, H., Luo, J., Fan, P., 2019. Lead-Free Formamidinium Bismuth Perovskites $(FA)_3Bi_2I_9$ with Low Bandgap for Potential Photovoltaic Application. Sol. Energy 177, 501–507.

Le Bail, A., 2005. Whole Powder Pattern Decomposition Methods and Applications. A Retrospection. cambridge.org.

Lee, M.M., Teuscher, J., Miyasaka, T., Murakami, T.N., Snaith, H.J., 2012. Efficient Hybrid Solar Cells Based on Meso-Superstructured Organometal Halide Perovskites. Science 338 (6107), 643–647.

Li, F., Fan, H., Wang, P., Li, X., Song, Y., Jiang, K.J., 2019. Improved Film Morphology of $(CH_3NH_3)_3Bi_2I_9$ via Cation Displacement Approach for Lead-Free Perovskite Solar Cells. J. Mater. Sci. 54 (14), 10371–10378.

Li, Y., Luo, X., Ding, T., Lu, X., Wu, K., 2020. Size- and Halide-Dependent Auger Recombination in Lead Halide Perovskite Nanocrystals. Angew. Chemie Int. Ed. 59 (34), 14292–14295.

Liu, M., Johnston, M.B., Snaith, H.J., 2013. Efficient Planar Heterojunction Perovskite Solar Cells by Vapour Deposition. Nature 501, 395–398.
Lyu, M., Yun, J.-H., Cai, M., Jiao, Y., Bernhardt, P.V., Zhang, M., Wang, Q., Du, A., Wang, H., Liu, G., Wang, L., 2016. Organic-Inorganic Bismuth (III)-Based Material: A Lead-Free, Air-Stable and Solution-Processable Light-Absorber beyond Organolead Perovskites. Nano Res. 9 (3), 692–702.
Ma, F., Li, J., Li, W., Lin, N., Wang, L., Qiao, J., 2017. Stable α/δ Phase Junction of Formamidinium Lead Iodide Perovskites for Enhanced near-Infrared Emission. Chem. Sci. 8, 800–805.
Malinkiewicz, O., Yella, A., Lee, Y.H., Espallargas, G.M., Graetzel, M., Nazeeruddin, M. K., Bolink, H.J., 2014. Perovskite Solar Cells Employing Organic Charge-Transport Layers. Nat. Photon. 8 (2), 128–132.
McClure, E.T., Ball, M.R., Windl, W., Woodward, P.M., 2016. Cs_2AgBiX_6 (X = Br, Cl): New Visible Light Absorbing, Lead-Free Halide Perovskite Semiconductors. Chem. Mater. 28 (5), 1348–1354.
McGehee, M.D., 2014. Perovskite Solar Cells: Continuing to Soar. Nat. Mater. 13, 845–846.
Mohammad, T., Kumar, V., Dutta, V., 2019. Electric Field Assisted Spray Coated Lead Free Bismuth Iodide Perovskite Thin Film for Solar Cell Application. Sol. Energy 182, 72–79.
Nie, W., Tsai, H., Asadpour, R., Blancon, J.C., Neukirch, A.J., Gupta, G., Crochet, J.J., Chhowalla, M., Tretiak, S., Alam, M.A., Wang, H.L., Mohite, A.D., 2015. High-Efficiency Solution-Processed Perovskite Solar Cells with Millimeter-Scale Grains. Science 347 (6221), 522–525.
Noel, N.K., Stranks, S.D., Abate, A., Wehrenfennig, C., Guarnera, S., Haghighirad, A.A., Sadhanala, A., Eperon, G.E., Pathak, S.K., Johnston, M.B., Petrozza, A., Herz, L.M., Snaith, H.J., 2014. Lead-Free Organic-Inorganic Tin Halide Perovskites for Photovoltaic Applications. Energy Environ. Sci. 7 (9), 3061–3068.
Noh, J.H., Im, S.H., Heo, J.H., Mandal, T.N., Seok, S.I., 2013. Chemical Management for Colorful, Efficient, and Stable Inorganic-Organic Hybrid Nanostructured Solar Cells. Nano Lett. 13 (4), 1764–1769.
Park, N.G., 2015. Perovskite Solar Cells: An Emerging Photovoltaic Technology. Mater. Today 18, 65–72.
Park, B.W., Philippe, B., Zhang, X., Rensmo, H., Boschloo, G., Johansson, E.M.J., 2015. Bismuth Based Hybrid Perovskites $A_3Bi_2I_9$ (A: Methylammonium or Cesium) for Solar Cell Application. Adv. Mater. 27 (43), 6806–6813.
Pazoki, M., Jacobsson, T.J., Hagfeldt, A., Boschloo, G., Edvinsson, T., 2016. Effect of Metal Cation Replacement on the Electronic Structure of Metalorganic Halide Perovskites: Replacement of Lead with Alkaline-Earth Metals. Phys. Rev. B 93, 144105.
Pazoki, M., Johansson, M.B., Zhu, H., Broqvist, P., Edvinsson, T., Boschloo, G., Johansson, E.M.J., 2016. Bismuth Iodide Perovskite Materials for Solar Cell Applications: Electronic Structure, Optical Transitions, and Directional Charge Transport. J. Phys. Chem. C 120 (51), 29039–29046.
Peng, J., Chen, Y., Zheng, K., Pullerits, T., Liang, Z., 2017. Insights into Charge Carrier Dynamics in Organo-Metal Halide Perovskites: From Neat Films to Solar Cells. Chem. Soc. Rev. 46, 5714–5729.
Piatkowski, P., Cohen, B., Javier Ramos, F., Di Nunzio, M., Nazeeruddin, M.K., Grätzel, M., Ahmad, S., Douhal, A., 2015. Direct Monitoring of Ultrafast Electron and Hole Dynamics in Perovskite Solar Cells. PCCP 17 (22), 14674–14684.
Ran, C., Wu, Z., Xi, J., Yuan, F., Dong, H., Lei, T., He, X., Hou, X., 2017. Construction of Compact Methylammonium Bismuth Iodide Film Promoting Lead-Free Inverted Planar Heterojunction Organohalide Solar Cells with Open-Circuit Voltage over 0.8 V. J. Phys. Chem. Lett. 8 (2), 394–400.
Sanders, S., Stümmler, D., Pfeiffer, P., Ackermann, N., Schimkat, F., Simkus, G., Heuken, M., Baumann, P.K., Vescan, A., Kalisch, H., 2018. Morphology Control of Organic-Inorganic Bismuth-Based Perovskites for Solar Cell Application. Phys. Status Solidi Appl. Mater. Sci. 215 (23), 1800409.
Shannon, R.D., 1976. Revised Effective Ionic Radii and Systematic Studies of Interatomic Distances in Halides and Chalcogenides. Acta Crystallogr. Sect. A 32 (5), 751–767.
Sheng, R., Ho-Baillie, A., Huang, S., Chen, S., Wen, X., Hao, X., Green, M.A., 2015. Methylammonium Lead Bromide Perovskite-Based Solar Cells by Vapor-Assisted Deposition. J. Phys. Chem. C 119 (7), 3545–3549.
Singh, T., Kulkarni, A., Ikegami, M., Miyasaka, T., 2016. Effect of Electron Transporting Layer on Bismuth-Based Lead-Free Perovskite $(CH_3NH_3)_3Bi_2I_9$ for Photovoltaic Applications. ACS Appl. Mater. Interfaces 8 (23), 14542–14547.
Singh, P., Rana, P.J.S., Dhingra, P., Kar, P., 2016. Towards Toxicity Removal in Lead Based Perovskite Solar Cells by Compositional Gradient Using Manganese Chloride. J. Mater. Chem. C 4, 3101–3105.
Slavney, A.H., Hu, T., Lindenberg, A.M., Karunadasa, H.I., 2016. A Bismuth-Halide Double Perovskite with Long Carrier Recombination Lifetime for Photovoltaic Applications. J. Am. Chem. Soc. 138 (7), 2138–2141.
Steinmann, V., Brandt, R.E., Chakraborty, R., Jaramillo, R., Young, M., Ofori-Okai, B.K., Yang, C., Polizzotti, A., Nelson, K.A., Gordon, R.G., Buonassisi, T., 2016. The Impact of Sodium Contamination in Tin Sulfide Thin-Film Solar Cells. APL Mater. 4 (2), 026103.
Stoumpos, C.C., Malliakas, C.D., Kanatzidis, M.G., 2013. Semiconducting Tin and Lead Iodide Perovskites with Organic Cations: Phase Transitions, High Mobilities, and near-Infrared Photoluminescent Properties. Inorg. Chem. 52 (15), 9019–9038.
Stranks, S.D., Snaith, H.J., 2015. Metal-Halide Perovskites for Photovoltaic and Light-Emitting Devices. Nat. Nanotechnol. 10, 391–402.
Sum, T.C., Mathews, N., Xing, G., Lim, S.S., Chong, W.K., Giovanni, D., Dewi, H.A., 2016. Spectral Features and Charge Dynamics of Lead Halide Perovskites: Origins and Interpretations. Acc. Chem. Res. 49 (2), 294–302.
Sun, S., Tominaka, S., Lee, J.H., Xie, F., Bristowe, P.D., Cheetham, A.K., 2016. Synthesis, Crystal Structure, and Properties of a Perovskite-Related Bismuth Phase, $(NH_4)_3Bi_2I_9$. APL Mater. 4 (3), 031101.
Tauc, J., 1968. Optical properties and electronic structure of amorphous Ge and Si. Mater. Res. Bull. 3, 37–46.
Volonakis, G., Haghighirad, A.A., Milot, R.L., Sio, W.H., Filip, M.R., Wenger, B., Johnston, M.B., Herz, L.M., Snaith, H.J., Giustino, F., 2017. $Cs_2InAgCl_6$: A New Lead-Free Halide Double Perovskite with Direct Band Gap. J. Phys. Chem. Lett. 8 (4), 772–778.
Wang, H., Tian, J., Jiang, K., Zhang, Y., Fan, H., Huang, J., Yang, L.M., Guan, B., Song, Y., 2017. Fabrication of Methylammonium Bismuth Iodide through Interdiffusion of Solution-Processed BiI_3/CH_3NH_3I Stacking Layers. RSC Adv. 7 (69), 43826–43830.
Wei, F., Deng, Z., Sun, S., Xie, F., Kieslich, G., Evans, D.M., Carpenter, M.A., Bristowe, P. D., Cheetham, A.K., 2016. The synthesis, structure and electronic properties of a lead-free hybrid inorganic–organic double perovskite $(MA)_2KBiCl_6$ (MA = methylammonium). Mater. Horiz. 3, 328–332.
Weller, M.T., Weber, O.J., Frost, J.M., Walsh, A., 2015. Cubic Perovskite Structure of Black Formamidinium Lead Iodide, α-$[HC(NH_2)_2]PbI_3$, at 298 K. J. Phys. Chem. Lett. 6 (16), 3209–3212.
Xiao, M., Huang, F., Huang, W., Dkhissi, Y., Zhu, Y., Etheridge, J., Gray-Weale, A., Bach, U., Cheng, Y.-B., Spiccia, L., 2014. A Fast Deposition-Crystallization Procedure for Highly Efficient Lead Iodide Perovskite Thin-Film Solar Cells. Angew. Chemie Int. Ed. 53 (37), 9898–9903.
Yang, B., Chen, J., Hong, F., Mao, X., Zheng, K., Yang, S., Li, Y., Pullerits, T., Deng, W., Han, K., 2017. Lead-Free, Air-Stable All-Inorganic Cesium Bismuth Halide Perovskite Nanocrystals. Angew. Chemie - Int. Ed. 56 (41), 12471–12475.
Yin, J., Ahmed, G.H., Bakr, O.M., Brédas, J.L., Mohammed, O.F., 2019. Unlocking the Effect of Trivalent Metal Doping in All-Inorganic CsPbBr 3 Perovskite. ACS Energy Lett. 4 (3), 789–795.
Zhang, Z., Li, X., Xia, X., Wang, Z., Huang, Z., Lei, B., Gao, Y., 2017. High-Quality $(CH_3NH_3)_3Bi_2I_9$. Film-Based Solar Cells: Pushing Efficiency up to 1.64%. J. Phys. Chem. Lett. 8 (17), 4300–4307.
Zhang, X., Wu, G., Gu, Z., Guo, B., Liu, W., Yang, S., Ye, T., Chen, C., Tu, W., Chen, H., Berlin, S.-V., 2016. Active-Layer Evolution and Efficiency Improvement of $(CH_3NH_3)_3Bi_2I_9$.-Based Solar Cell on TiO 2-Deposited ITO Substrate. Springer 9 (10), 2921–2930.
Zhou, Z., Pang, S., Ji, F., Zhang, B., Cui, G., 2016. The Fabrication of Formamidinium Lead Iodide Perovskite Thin Films via Organic Cation Exchange. ChemComm. 52, 3828–3831.